



Simultaneous PIV/PTV velocimetry technique in a turbulent particle-laden flow

Mehdi Elhimer, Olivier Praud, Moise Marchal, Sébastien Cazin, Rudy Bazile

► To cite this version:

Mehdi Elhimer, Olivier Praud, Moise Marchal, Sébastien Cazin, Rudy Bazile. Simultaneous PIV/PTV velocimetry technique in a turbulent particle-laden flow. *Journal of Visualization*, 2016, 19 (75), pp.1-16. 10.1007/s12650-016-0397-z . hal-03516284

HAL Id: hal-03516284

<https://hal.science/hal-03516284>

Submitted on 7 Jan 2022

HAL is a multi-disciplinary open access archive for the deposit and dissemination of scientific research documents, whether they are published or not. The documents may come from teaching and research institutions in France or abroad, or from public or private research centers.

L'archive ouverte pluridisciplinaire **HAL**, est destinée au dépôt et à la diffusion de documents scientifiques de niveau recherche, publiés ou non, émanant des établissements d'enseignement et de recherche français ou étrangers, des laboratoires publics ou privés.



Open Archive TOULOUSE Archive Ouverte (OATAO)

OATAO is an open access repository that collects the work of Toulouse researchers and makes it freely available over the web where possible.

This is an author-deposited version published in : <http://oatao.univ-toulouse.fr/>
Eprints ID : 16630

To link to this article : DOI:10.1007/s12650-016-0397-z
URL : <http://dx.doi.org/10.1007/s12650-016-0397-z>

<p>To cite this version : Elhimer, Mehdi and Praud, Olivier and Marchal, Moise and Cazin, Sébastien and Bazile, Rudy <i>Simultaneous PIV/PTV velocimetry technique in a turbulent particle-laden flow</i>. (2016) Journal of Visualization, vol. 19 (n° 75). pp. 1-16. ISSN 1343-8875</p>
--

Any correspondence concerning this service should be sent to the repository administrator: staff-oatao@listes-diff.inp-toulouse.fr

M. Elhimer · O. Praud · M. Marchal · S. Cazin · R. Bazile

Simultaneous PIV/PTV velocimetry technique in a turbulent particle-laden flow

Abstract In a three-dimensional two-phase flow, accessing the velocity fields of the two phases simultaneously is challenging. Nevertheless, information about the local relative motion between the two phases is particularly valuable to quantify the inter-phase interactions. In this article, the dynamics of neutrally buoyant finite-sized particles embedded in a three-dimensional turbulence is investigated using a simultaneous particle image velocimetry (PIV) and particle tracking velocimetry (PTV) measurement technique based on optical discrimination of the two phases prior to image acquisition. The implementation of this dual whole-field velocimetry technique is presented and detailed. With this technique, we were able to measure the instantaneous and local velocity differences between the particles and the underlying fluid. Our results show that, whereas the single-point velocity statistics of the two phases are very similar, the particles often have different local velocity than the velocity of the neighboring fluid. The relative velocity increases with the relative size of the particle to the Kolmogorov scale. In addition, the relative velocity exhibits an intermittent distribution.

Keywords Particle-laden flow · Optical discrimination · Toward grid turbulence · Particle image velocimetry · Particle tracking velocimetry

1 Introduction: aim and scope of the study

Turbulent particulate flows are present in many natural and industrial processes. Transport of sediment in rivers and estuaries, convection of pollutants in the atmosphere (Weil et al. 1992), bio convection of zoo-plankton (Schmitt and Seuront 2008), gravity and turbidity currents near coastal shores, and pyroclastic flows from volcanic eruptions are a few examples that can be encountered in natural phenomena. In industry, processes involving flows of particles are numerous, including fluidized bed reactors, the treatment of waste materials in clarifiers, food processing, and ink technologies to name a few. A good understanding and modelling of such complex flows is naturally of great use from scientific and engineering perspectives, as they directly impact the environment we live in. In all these examples, the interaction between the dispersed phase and the carrier flow is a dominant phenomenon which is important to understand in a fundamental way.

Despite their abundance, still little is known about particle–turbulence interaction. However, the number of experimental, theoretical, and numerical studies is steadily increasing, mainly dealing with the particle dynamics and their influence on the turbulence (see Poelma et al. (2006), Balachandar and Eaton (2010), Monchaux et al. (2012) for recent reviews). Nevertheless, theoretical or numerical models still need consistent experimental data for their validation. In this paper, we present and use a method to obtain

conditional statistics in a particle-laden turbulent flow using optical whole-field measurements. It consists of a dual camera particles images velocimetry (PIV)/particles tracking velocimetry (PTV) system which allows simultaneous measurement of the velocities of both phases. The properties of the carrier flow are obtained through PIV measurements, while PTV is dedicated to velocity measurement of the dispersed phase. Through this technique, we present quantitative measurements of the local and instantaneous relative velocities between the two phases, which are particularly valuable to quantify the inter-phase interactions.

Particle image velocimetry is now widely used to measure the instantaneous velocity fields of fluid flows. The basic principle of the PIV technique is to measure the most probable displacement of an ensemble of tracer particles of a given flow between two successive camera frames. The images are usually cross-correlated (in the physical space or Fourier space) to obtain the velocity field. On the other hand, particle tracking velocimetry (PTV) involves tracking the motion of individual particles between two successive camera frames to obtain their instantaneous velocities. This technique is based on identification, coordinate determination, and temporal matching of each individual particle.

Several studies are reported in the literature for combining these two velocimetry techniques. One set of techniques is based on the separation of particles and fluid tracers images during the post-processing of the acquired image by means of various image processing algorithms (Khalitov and Longmire 2002; Kiger and Pan 2000; Vignal 2006). These methods are based on the recognition of the large particles and their elimination from the image prior to the cross-correlation analysis. The main advantage of these methods is the simplicity of the associated set-up, since a single monochromatic camera is needed. Their drawback is the appearance of “holes” at the location of the eliminated particles images which make it difficult to measure the velocity of the fluid sufficiently close to particles positions. Another set of methods is based on optical discrimination. When each phase emits light at different wavelengths, a color camera can be used to discriminate the two phases by splitting the RGB channels (Hagiwara et al. 2002). Otherwise, a dual set-up camera can be used. Each camera is equipped with an appropriate filter to receive the light from one phase only. This latter method has been successfully used by Poelma (2004) to study the modification of an isotropic turbulence due to the presence of the particles (see also Poelma et al. 2006, 2007). A similar technique will be used in this study to measure the local relative velocity between the large particles and the fluid flow and to analyse its statistics.

The studies on the particle-laden flows have been mainly concerned with particles having a size significantly smaller than the smallest length scale of the flow, and a density significantly larger than the fluid density (Lu et al. 2010; Bec et al. 2006; Squires and Eaton 1991; Aliseda et al. 2002; Yoshimoto and Goto 2007). This is partially due to the relative simplicity of their equation of motion, since the dominant effects are the drag force and gravity. Albeit its simplicity, the dynamic of these particles in a turbulent flow has shown a rich phenomenology, chiefly depending on the particle Stokes number, St . Nevertheless, many particle-laden flows involve particles with a relatively large size and small density. In this case, the equation of motion of the particle is fully non-linear, in opposition to the previous case of dense and point-like particles. The specific case of neutrally buoyant particles is of interest as a reference, because it isolates finite-size effects. Since $\rho_p = \rho_f$, the particles dynamics are expected to be mainly affected by spatial filtering of the velocity field, instead of the dominant temporal filtering as in the case of small and heavy particles.

In the case of neutrally buoyant particles, the relationship between a particle velocity and the surrounding fluid velocity can be expressed through the first-order Faxen correction. From this, a relationship between the particles velocity statistics and their size can be derived (Calzavarini et al. 2012). Results from direct numerical simulations (DNS) show that this scaling matches the results of the simulations for diameters up to five times the Kolmogorov length scale (Homann and Bec 2010). However, this scaling has not been validated experimentally. Qureshi et al. (2007) tracked inflated soap bubbles in grid generated turbulence using acoustic Doppler velocimetry. No influence of particles diameter was found on particles velocity variance, which fluctuates slightly and with no clear trend around the value of the fluid velocity variance. For a two-dimensional chaotic flow, Ouellette et al. (2008) measured simultaneously the velocities of the particles and the surrounding fluid. Their results show that both the particles diameter and the Reynolds number affect the statistics of the velocity differences between the particles and the surrounding fluid. However, no precise scaling was derived from their results.

This paper focuses on the dynamics of neutrally buoyant, finite-size particles embedded in a three-dimensional turbulent flow. Using an innovative velocimetry set-up based on optical discrimination, we measured simultaneously the velocities of the particles and the surrounding flow. The paper is organized as follows. In Sect. 2, the experimental set-up is described. The optical measurement technique is presented in Sect. 3. Finally, Sect. 4 is dedicated to the analysis of the statistics on the relative motion between the two phases.

2 Experimental set-up

2.1 Experimental apparatus

The experiments were performed in a rectangular glass tank ($0.5 \text{ m} \times 0.5 \text{ m} \times 0.7 \text{ m}$) filled with filtered water similar to the one used by Elhimer et al. (2011). A turbulent flow is generated by moving upward a square grid at a constant velocity $U = 1 \text{ m.s}^{-1}$ along a stroke of 0.5 m . Afterwards, the turbulent flow is let to decay freely until the next stroke. The tank is equipped with a surface tray, so the flow is not perturbed by the free surface motion. A schematic representation of the turbulence generator is shown in Fig. 1.

A common drawback of confined turbulence generation is the existence of a persistent large-scale circulation flow. Fernando and De Silva (1993) put forward a design criterion to reduce this flow by choosing judicious near wall conditions: the grid needs to obey to reflective symmetry with reference to the walls of the tank. This symmetry criterion has been respected when designing the grid: the spacing between the wall and the nearest parallel bar is half a grid mesh size $M/2$. The grid is made of square rods of sides 1 cm with a mesh size $M = 4.5 \text{ cm}$, and a solidity $\sigma = 0.395$ which is close to the solidity of grids usually used in wind tunnels for generating isotropic turbulence (Mohamed and Larue 1990). The grid is attached to a linear slide which is set in motion by an electrical motor (LENZE-MCS12H35). This motor is synchronized to the image acquisition system through a homemade and specifically designed synchronization box. This box generates a first signal to trigger one grid motion cycle. During one cycle, the grid first moves down slowly at a velocity of 0.1 m.s^{-1} , then it moves up at a velocity of 1 m.s^{-1} to generate the turbulence. The box generates a second delayed signal to trigger camera acquisition during a user-specified time interval (acquisition window). These two signals are synchronized with the LASER source.

In our experiments, the initial time $t.U/M = 0$ is taken at the end of grid stroke. The PIV measurements are triggered at $t.U/M = 40$, where the turbulence is considered to be homogeneous and isotropic (Morize et al. 2005). To avoid sustaining the mean flow, the delay between two successive grid motion cycles must be sufficiently large compared with the characteristic time of the generated flow, which scales as M/U . A delay of $1000 M/U$ which corresponds to 54.4 s was found long enough to ensure that the flow generated from the previous grid motion has sufficiently decayed.

2.2 Particles

The solid particles used as dispersed phase were kindly provided by H. Didelle from LEGI¹. Prior to their use, the particles were sieved to obtain a distribution of diameters d_p in the range $1.12\text{--}1.8 \text{ mm}$. The diameters of a sample of 58 particles was measured from magnified images and illustrated in Fig. 2. The measured diameters are shown to vary between 1 and 1.5 mm , the most frequent value being close to 1.4 mm . As we shall see later, the particles diameters are, therefore, significantly larger than the Kolmogorov length scale of the turbulent flow in the water tank. The volume fraction (or volume loading) of the particles in the water tank was close to $\Phi_v = 3.10^{-3}$; the choice of such a small loading is intended to make negligible both turbulence modulation and inter-particle hydrodynamic interactions.

To achieve a density match between the two phases, water density is increased by salt addition until the particles remain suspended in the tank, and their settling velocity is small compared with the fluid velocity. The typical concentration of NaCl is $5.5 \text{ wt } \%$ and the water density is measured using an hydrometer (Alla France). However, since the density of salt water slightly changes with temperature, pressure, and evaporation, the density is adjusted before every experiment by addition of brine or fresh water. The water is filtered before filling the tank to eliminate both salt agglomerates and dust particles. The settling velocity of the particles in the still salt water is measured by tracking the particles in successive images acquired by a camera and is found to be $V_s = 6.76.10^{-4} \text{ m.s}^{-1}$ in average for a measured water density of $\rho_f = 1.037 \text{ g.ml}^{-1}$. This settling velocity is thus negligible compared with the fluid velocity r.m.s u' , since $V_s/u' = 2.24.10^{-2}$ at $t.U/M = 66.6$. Particles buoyancy is thus considered to be negligible in comparison with the other forces.

¹ Laboratoire des Ecoulements Géophysiques et Industriels, 1209-1211 rue de la piscine, Domaine Universitaire, 38400 Saint Martin d'Hères. They were prepared from polystyrene beads by a process of cooking, which decrease slightly the density below 1.04 g.cm^{-3} .

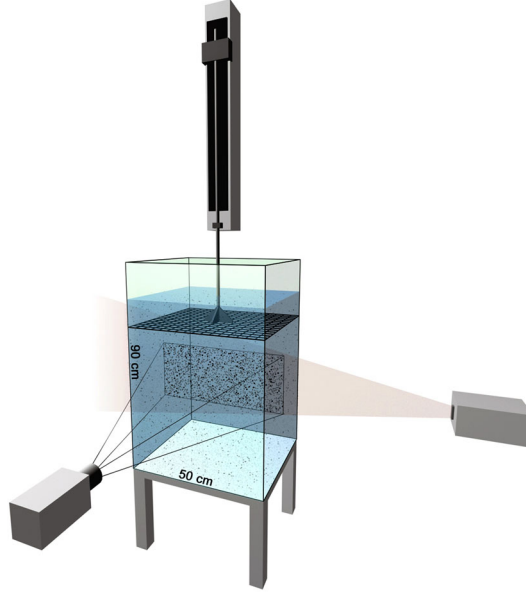


Fig. 1 Scheme of the towed grid turbulence generator, with the PIV set-up. To generate the turbulent flow, the grid moves upward in the water tank and the turbulence then decays freely until the next stroke of the grid

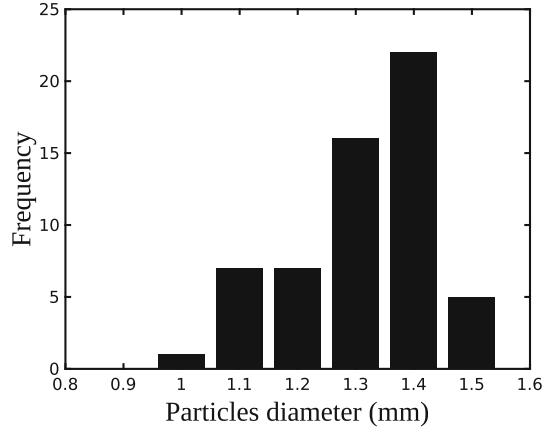


Fig. 2 Histogram of the diameters of the polystyrene particles used as dispersed phase in our experiments

3 Simultaneous velocimetry

3.1 Optical discrimination principle and set-up

Various phase discrimination techniques are reported in the literature (Khalitov and Longmire 2002; Kiger and Pan 2000; Blois et al. 2015; Vignal 2006; Poelma et al. 2006). One particular set of these techniques is optical discrimination, based on the difference on the wavelength of the light emission of each phase.

This method is implemented using, for the PIV tracers, a fluorescent dye encapsulated in the tracer particles. The fluorescent dye absorbs energy at the laser wavelength and emits light at a longer wavelength, while the large particles scatter the incoming light at the same wavelength. Distinguishing fluorescent light from the scattered light requires a two camera set-up shown in Fig. 3. One camera (PIV camera) is equipped with an appropriate cut-off filter that transmits only the fluorescent light emitted by the tracers. The scattered light from the large particles is recorded by a second camera (PTV camera).

In our experiments, the flow was illuminated by a vertical light sheet, which is generated by a double cavity Nd:YAG pulsed LASER (Spectra-Physics—Quanta-Ray PIV 400) with an energy output of 200 mJ for each cavity at wavelength $\lambda = 532$ nm. The light sheet is formed by first focusing the laser beam (with a

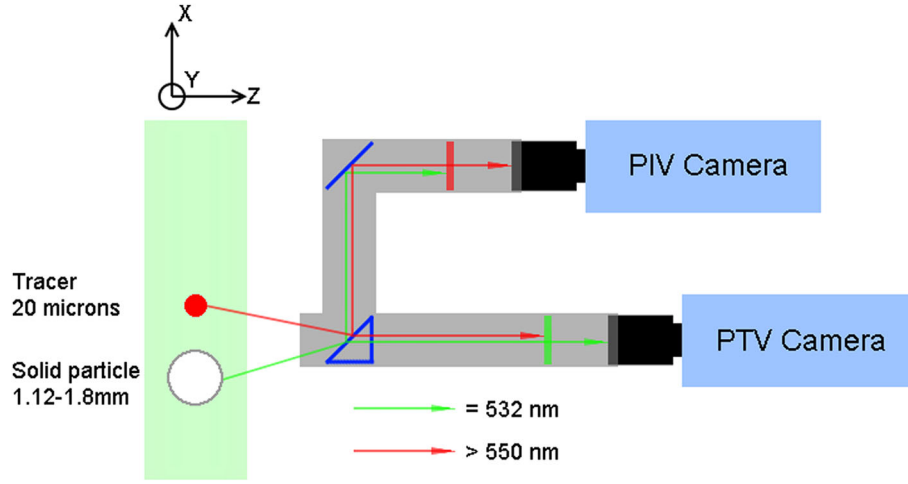


Fig. 3 Simultaneous velocimetry set-up scheme. The fluorescent tracers absorb the incoming light at the LASER source wavelength 532 nm and re-emit it at a higher wavelength > 550 nm. The PIV dedicated camera is equipped with an appropriate cut-off filter, thus receiving only the light emitted by the tracers

diameter of nearly 8 mm) using a spherical lens of focal length 1 m. The beam is then expanded in the vertical direction by means of a cylindrical lens of focal length -12 mm. The light sheet thickness, measured at the walls of water tank with a photosensitive paper, is close to 2 mm. This value ensures that the thickness is smaller than the spatial resolution of the PIV measurement (6.25 mm). It is also large enough, so that the loss of particles due to the out of plane motion is only a small percentage (less than 20 % if we consider an isotropic turbulence). The light sheet thickness variation across the tank is found to be less than 1 mm, and we can, therefore, estimate the variation across the field-of-view ($12.5 \text{ cm} \times 10 \text{ cm}$) to be less than 0.5 mm.

Besides the large particles, the flow was seeded with spherical fluorescent PPMA tracers from DANTEC (FPP-RhB-35) of size $20\text{--}50 \text{ }\mu\text{m}$ and of density 1.19 g.cm^{-3} . We can derive an estimate of the characteristic time, τ_t , needed for tracers to attain velocity equilibrium with the fluid using Stokes drag: $\tau_t = d_t^2 \rho_t / 18 \mu_f$, where d_t is the diameter, ρ_t the density of the tracer particles, and μ_f the dynamic viscosity of the fluid. Using $50 \text{ }\mu\text{m}$ diameter tracers, the relaxation time is $1.5 \cdot 10^{-4} \text{ s}$ which is much shorter than the characteristic time scale of the flow. The settling velocity given by $d_t^2 \Delta \rho_t / 18 \mu_f$, where g is gravitational acceleration and $\Delta \rho$ is the density difference between the fluid and the tracers, is close to $2 \cdot 10^{-4} \text{ m.s}^{-1}$. This is much lower than the typical measured velocity of the fluid. We can, therefore, consider that the tracers passively follow the fluid motion. These tracers are made with Rhodamine B fluorescent dye homogeneously distributed over the entire particle volume. The excitation and emission spectra of the Rhodamine B (Fig. 4) show that LASER wavelength $\lambda = 532 \text{ nm}$ is within the excitation range, while the emission signal is non-negligible only for larger wavelength.

The fluorescent and scattered signals are transmitted through an imaging system to be caught by two identical sensicam cameras (PCO—Sensicam 1280×1024 pixels at 8 fps, 12 bits). The images were recorded in two successive frames (synchronized to the LASER pulses). The maximum frame rate of the camera in the double frame mode is limited to 8 Hz, whereas each cavity emits light pulses at a frequency of 10 Hz. The acquisition frequency of the double frame CCD sensor is then set to 5 Hz per frame, so every two laser pulse is skipped.

The cameras were both equipped with lenses with a focal length of 105 mm. Both were focused on the same field-of-view using a view field splitter made at the IMFT. It consists of a beam splitter plate and a mirror, both placed at 45° from the cameras optical axis as illustrated in Fig. 3. In our experiments, the field of view of the camera was set to a size of $12.5 \text{ cm} \times 10 \text{ cm}$. The PIV camera was equipped with 550 nm cut filter (OD:6.5—LaVision) and its aperture was set to # 4. The PTV camera was equipped with a band-pass filter (532 nm—bandwidth 10 nm—LaVision) and a set of three neutral density filter (ND2, ND4 and ND8—KENKO). Its aperture was set to # 32. The laser intensity has to be high enough for the fluorescent tracers to be imaged by the PIV camera. The neutral density filters and a small aperture are then used to reduce the scattering intensity of the dispersed phase imaged by the PTV camera to not overexpose the PTV images. Using a f#32, the diffraction limited image diameter, which can be calculated using

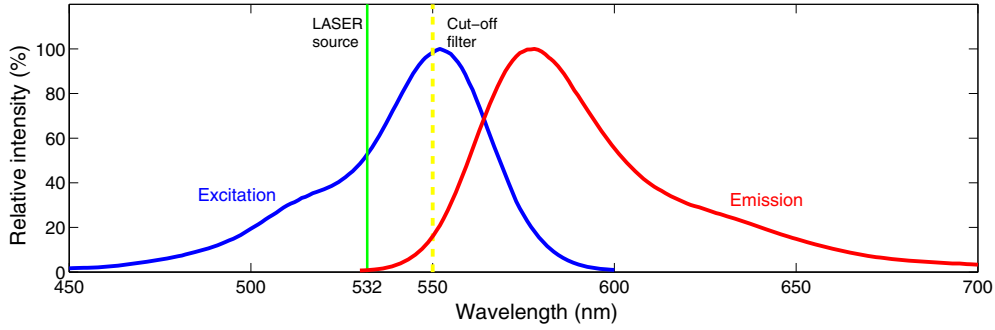


Fig. 4 Excitation and emission spectra of the Rhodamine B fluorescent dye. Data from Thermo Fisher scientific Inc

$d_{\text{diff}} = 2.44f\#(M + 1)\lambda$. With $\lambda = 532$ nm and a magnification $M = 0.1$, this yields $d_{\text{diff}} = 41$ μm , which corresponds to 4 pixels. The image of the dispersed phase particle is then given by the convolution of the point spread function with the geometric image of the particle and one can estimate the particle image diameter using $d_{\text{eff}} = \sqrt{(Md_p)^2 + d_{\text{diff}}^2}$. With $d_p = 1.5$ mm, this yields an effective diameter very close to Md_p . In addition, no fringe of diffraction are observed around the PTV particles images. We can then consider that there is very little effect of the of diffraction on imaging the PTV particles.

3.2 Fluid velocimetry: PIV

As can be seen in Fig. 5, large particles appear on the image recorded by the PIV camera. The presence of both fluid tracers and dispersed phase particles on the fluid phase images may have multiple origins, such as coating of the large particles by the fluorescent ones, low-quality filters, and transmission of 532 nm light through the cut filter. To identify the possible source of the observed cross-talk, exact same experiments and image acquisitions were performed with and without fluorescent tracers. All the optical and physical parameters were kept constant (LASER power, exposure time, optical set-up, and particles size). In the absence of tracers, we did not observe any disperse phase particles images in the PIV images, which indicates that the scattering by the 1 mm polystyrene beads of the fluorescent light emitted by the tracers is responsible for the observed cross-talk.

The presence of these particles images may influence the cross-correlation results and they need to be removed prior to cross-correlation. The PIV images' histograms do not exhibit a double peak structure which indicates that the gray levels of those particles images belongs to the same range than the tracers images. However, close inspection reveals that those particles are associated with gray levels smaller than

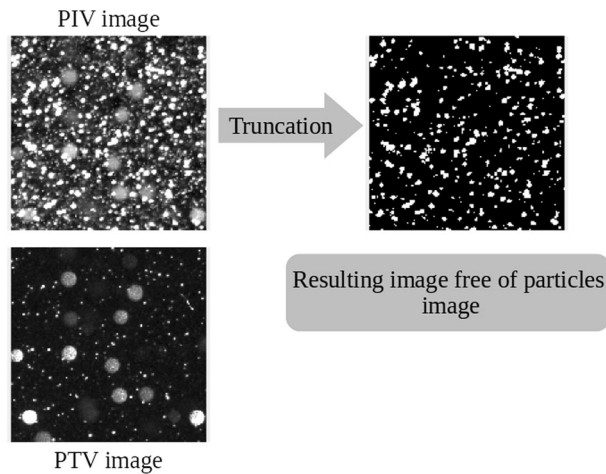


Fig. 5 Portion of the original PIV image, showing the presence of particles images in PIV images, with the corresponding PTV image and the PIV image after truncating its histogram. To facilitate the illustration, the histogram of the PIV images, before and after the processing, was adjusted to highlight the presence of the large particles. From the 12 bit image, only the gray levels in the range [130–420] are displayed

most of the tracers but do not exceed the value $I_b = 375$. We, therefore, eliminate dispersed particles from images by truncating the histogram of the PIV images at I_b and setting to zero all the pixels with a gray level below I_b . The pixels set to zero (“holes”) include not only large particles, but also the background and weakly illuminated tracers. This procedure does not propagate the presence of the large particles on the resulting images and preserves sufficient gray levels to ensure the quality of the cross-correlation. The main drawback of this discrimination technique is that the truncation results in images with a large number of zero-valued pixels. The cross-correlation analysis, therefore, requires the use of large interrogation windows to have sufficient number of tracers within the interrogation windows. An example of the resulting particle free PIV images is shown in Fig. 5.

A cross-correlation analysis is then performed on the PIV images to measure the tracers displacement between two camera frames. We used the CIV (correlation image velocimetry) algorithm introduced by Fincham et al. (1991) which is, like most of recent PIV algorithm, based on a pattern matching technique. Each pair of images is treated as described by Fincham and Spedding (1997), Fincham and Delerce (2000) and the procedure is briefly recalled here. Each frame is subdivided into small pattern boxes of size B pixels. The ensemble of the pixels contained in each pattern box in the first frame is directly cross-correlated in real space with a shifted same size pattern box in the second frame, within a search box of size S pixels. For each shift, a correlation coefficient is associated, and the shift corresponding to the largest local maxima of this function is the most likely mean integer displacement of the tracers contained in the pattern box. This coarse approximation is then refined to give a sub-pixel estimate of the displacement through the use of a peak fitting function. Like Fincham and Spedding (1997) and Fincham and Delerce (2000), the thin-shell smoothed spline functions described by Spedding and Rignot (1993) is chosen for this analysis. A vector correcting routine is implemented, which compares each vector with its neighbors by computing the relative deviations in both magnitude and direction, the most deviant neighbor is discarded (Fincham and Spedding 1997). Velocity data are then re-interpolated with the same smoothing spline used in the peak fit.

Like many PIV algorithms, a hierarchical scheme, in which information from successive passes is used to refine the displacement measurement, is implemented. The results from this first iteration are improved in a second iteration with reduced pattern box search zone. In addition, the prior knowledge of the local velocity gradient tensor is used to locally deform and rotate the interrogation boxes. In the first pass, the size of the interrogation window was set to 128 pixels. For the final iteration, we set the pattern box size at $B = 64$ pixels with an overlap of 75 % between adjacent pattern boxes. The spatial resolution associated with the finite size of the interrogation window and defined by the size of this sampling volume (Adrian 1997) is 6.25 mm, whereas the grid resolution of the resulting velocity field, defined by the distance between two vectors, is 1.56 mm. The average number of particles in the final interrogation box is estimated at 22. The particles were counted based on the criteria that they have at least four connected pixels with intensities greater than an intensity threshold of 380. This density number is in the range for which double pulse laser systems operate best (Keane and Adrian 1990).

The accuracy of the used algorithm on the measured displacement was estimated by Fincham and Delerce (2000) to be less than 0.1 pixels and actual hardware tests using real particles “frozen” inside a clear resin block, along with tests on stagnant fluid, showed that under optimum conditions, the measured mean r.m.s. error in velocity is less than 2 %. In addition, an a posteriori uncertainty quantification was also performed to determine the uncertainty of the PIV measurement from the correlation peak ratio Q (Charonko and Vlachos 2013; Sciacchitano et al. 2015). Since the algorithm only retains displacement with $Q > 1.3$ (displacement with $Q < 1.3$ are considered as outliers), we can estimate the upper bound of the uncertainty at 0.3 pixel.

3.3 Particles velocimetry: PTV

The particle tracking velocimetry (PTV) technique involves tracking the motion of individual particles between two successive camera frames. First, each particle image is detected and localized on each camera frame. Then, the two particles images are “matched”, i.e., identified as belonging to the same particle without ambiguity. The difference between the positions of the two particles images gives the particle displacement between the two frames. Those three stages of the PTV process are illustrated in Fig. 6 and are detailed in the following.

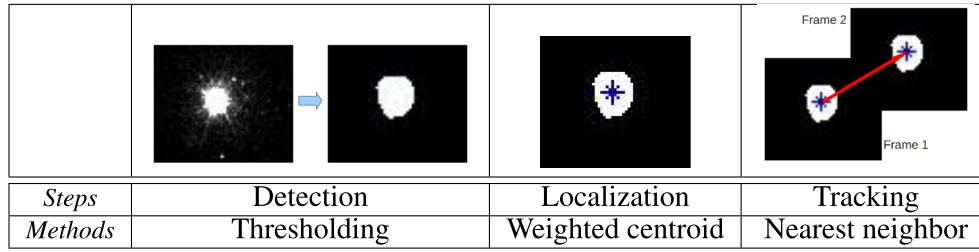


Fig. 6 Particle tracking velocimetry process

3.3.1 Particle detection

The common procedure for detecting particles images is by means of image thresholding. In this method, all pixels with gray scales exceeding a defined threshold value are labeled as belonging to particle images and the remaining pixels are labeled as belonging to the image background. The pixels belonging to particles images are tagged 1 and the background pixels are tagged 0. The resulting images are hence called binarized images (Adrian and Westerweel 2011).

Visual inspection shows that the acquired images contain a large number of particle images originating from the outside of the measurement volume. The particles included in the thickness of the laser sheet are considered to be the largest and the most illuminated particle images, whereas the particles outside the Laser sheet are less luminous. To remove these particles, we set the grayscale threshold, based upon visual inspection, to 625 (while the maximum gray scale is 4096) and we considered only particles images having an equivalent diameter larger than five pixels.

Other methods for particles detection have been reported in the literature. Takehara and Etoh (1999) have introduced the mask correlation method. It involves cross-correlating the entire image with a “mask”, i.e., a model particle image with a Gaussian illumination profile. The positions of the correlation maxima are the estimations of the particles positions in the image. The authors show that this method works only when the particles images’ illumination profile is nearly Gaussian, which is not the case in our experiments, since the particle images’ grayscale saturates over several pixels. Another method used by Khalitov and Longmire (2002) is based on the detection of local maxima of the illumination in the images. This method cannot be used in our experiments for the same reason.

3.3.2 Position determination

The position of each detected object is defined as the position of its centroid defined as position of the barycenter of the ensemble of the pixels belonging to the object weighted by their grayscale values. If the object has a circular shape and a symmetrical illumination profile, the centroid position is an unbiased estimation of particles images location. Asymmetry in both shape and illumination profiles yields to an ambiguity on the centroid position and thus introduces a bias on the estimation of the particle location (Adrian and Westerweel 2011).

An estimation of the circularity of the binarized particle image is needed to evaluate the bias on the centroid position. This is provided by the eccentricity of the ellipse that has the same second moment as the binarized particle image. The eccentricity is the ratio of the distance between the foci of the ellipse and its major axis length. It ranges from $\varepsilon = 0$ for a circle to $\varepsilon = 1$ for a parabola. An histogram of the particle images eccentricities is shown in Fig. 7 for the two camera frames. The most probable value of eccentricity is close to $\varepsilon = 0.3$. All the particles with an eccentricity above a critical value $\varepsilon = 0.6$ are not further considered in the tracking procedure. Examples of erroneous displacement rejected by this criterion are illustrated in Fig. 8. In most cases, large eccentricity particle images originate either from an occultation of a particle by other particles or because two particles are too close to each other and form a single object on the binarized image. The use of the eccentricity criterion allows to detect and eliminates these cases.

When the bias errors are identical for particle image centroids on both frames, they cancel each other. Thus, the measured particle displacement (which is the difference of the two centroid positions) is unaffected by this bias (Adrian and Westerweel 2011). However, a significant change of the particle shape introduces a bias on the measurement of the displacement. An estimate of the change of the shape of the binarized particle image between the two frames is given by the ratios of the eccentricities and diameters

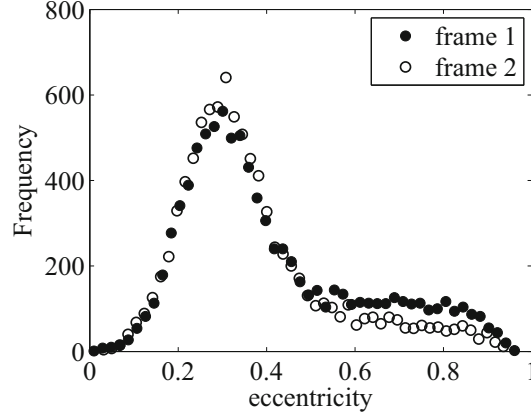


Fig. 7 Histogram of the measured eccentricity of the detected particle image on the two camera frames

frame1	frame2	displacement (pixels)	eccentricity
		17.5	0.83
		19.3	0.84
		15.1	0.85

Fig. 8 Examples of high eccentricities leading to erroneous centroid localizations and displacements. Dots represent the position of the weighted centroid of the object

between the two frames. Figure 9 shows the distribution of those ratios. The eccentricity and diameter are shown to be only slightly changed between the two frames. Thus, the measured particle displacement is often unaffected by bias on the particle centroid.

3.3.3 Pair matching

The pair matching involves identifying for each particle image in the first frame and the corresponding particle image in the second frame. In the present experiments, the displacement of the particle images is small with respect to the mean spacing between neighboring particle images. Therefore, each particle image in the first frame is paired with its closest neighbor in the second frame (Adrian and Westerweel 2011). For each detected particle position \mathbf{x}_p of image n , we find any particle p' of image $n + 1$, whose position $\mathbf{x}_{p'}^{n+1}$ lies within a circle of radius $R = 20$ pixels, i.e., $|\mathbf{x}_{p'}^{n+1} - \mathbf{x}_p^n| < R$. We then select the closest event for the pairing. For particle p whose position, \mathbf{x}_p^n , in image n moves to position \mathbf{x}_p^{n+1} in the subsequent image $n + 1$, its velocity is $\mathbf{v}_p^n = (\mathbf{x}_p^{n+1} - \mathbf{x}_p^n) / \Delta t$ where Δt is the time between frames.

Two different tests have been performed to validate the tracking algorithm. In the first one, a known displacement is applied to all the pixels of an image from the PTV camera. The displacement computed by the algorithm D_{meas} is compared with the imposed displacement D_{imp} , and the average difference $\langle D_{\text{meas}} - D_{\text{imp}} \rangle$ is computed over 300 images. The results for different values of the imposed displacement D_{imp} are reported in Fig. 10a. The discrepancy is found to be smaller than one pixel on average for values of D_{imp}

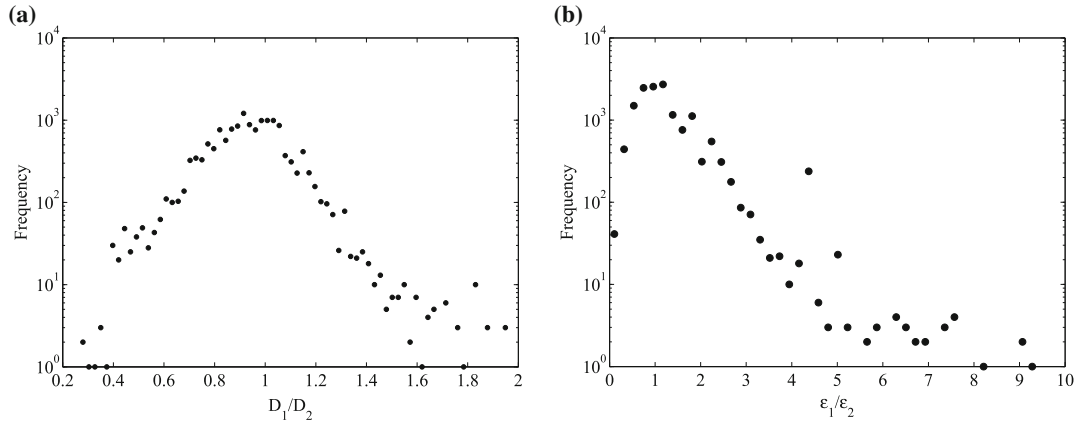


Fig. 9 Histograms of the particle images diameters and eccentricities ratios between the two frames D_1/D_2 and $\varepsilon_1/\varepsilon_2$. For the two ratios, the most probable value is 1

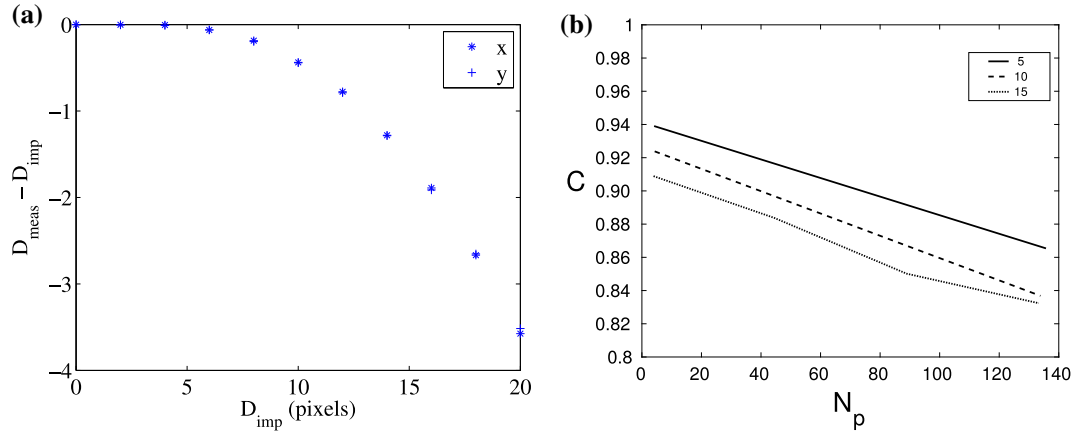


Fig. 10 **a** Imposed displacement D_{imp} against its difference with the mean measured displacement D_{meas} . **b** Rate of correct particles matching C versus the number of particles per image N , for different maximal displacements in pixels D_{max}

smaller than ten pixels. The average discrepancy then grows for larger imposed displacements. Since the tracking algorithm matches each particle in the first frame to its closest neighbor in the second frame, an erroneous matching always leads to an underestimation of the actual displacement. Therefore, the average measured displacement is always smaller than the imposed displacement.

A second test is to generate synthetic particle images with gaussian grayscale profiles. These images were submitted to random displacements. The test was performed for different numbers of particles in the images N_p and different maximal displacements D_{max} . For each value of N_p and D_{max} , the ratio C of the number of correct matchings to the total number of matchings is computed. As shown in Fig. 10b, more than 90 % of the particles are correctly matched when the images contain less than 60 particles, even for D_{max} as large as 15 pixels. In our experiments, the images contain less than 15 particles in average and the average displacement is between 5 and 7 pixels. Thus, with this tracking algorithm, the matching rate is expected to be larger than 90 %.

3.3.4 Results example

An example of the results obtained from the simultaneous velocimetry is shown in Fig. 11. The particular advantage of this technique is remarkable: the velocity of the particles and the nearest fluid tracers can be measured simultaneously, and the presence of the particles do not yield “holes” in the fluid velocity field. Consequently, this velocimetry method is suited for the measurement of the differences between the velocity of each particle and the surrounding fluid.

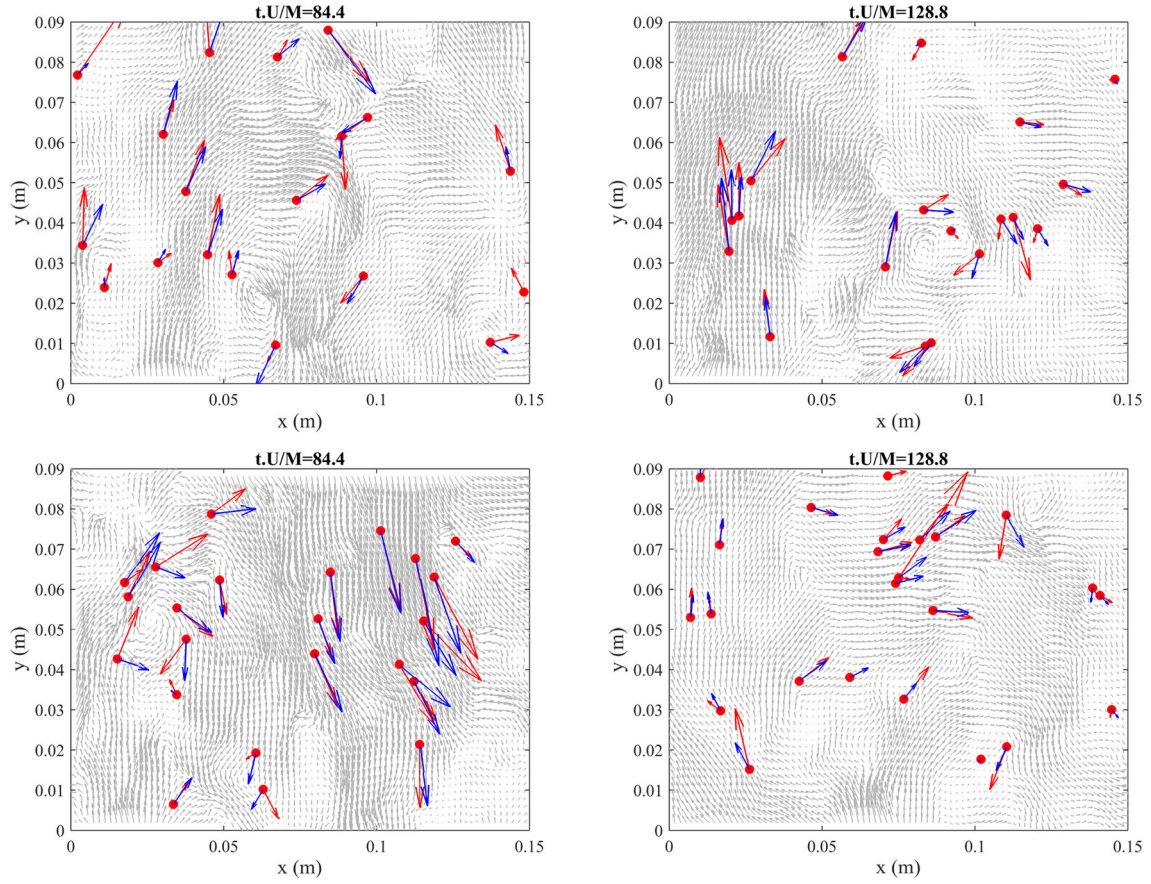


Fig. 11 Example of the two phase velocity fields at two decay stages. The fluid velocity vectors are in gray, particle velocity vectors are in red, and fluid velocity vectors at the location of the particles are in blue. Red and blue arrows are enlarged four times to facilitate their visualization

4 Results

First, we compare the particles size d_p and the particle viscous relaxation time τ_p to the Kolmogorov length and time scales, respectively, for different stages of the decay. The Kolmogorov time scale is defined as $\eta = (\nu^3/\epsilon)^{1/4}$, where ν is the kinematic viscosity of the fluid and ϵ is the turbulence dissipation rate. From PIV measurements, we get the velocity gradients from which ϵ is computed. The Kolmogorov length scale increases during the decay of the turbulence. Therefore, the ratio $\Phi = d_p/\eta_k$ decreases with time from 4 to 3, as shown in Fig. 12. In this range, the finite-size effects on particle dynamics are noticeable (Homann and Bec 2010). The particle inertia is characterized by the Stokes number ($St = \tau_p/\tau_k$) which compares the Kolmogorov time scale $\tau_\eta = (\nu/\epsilon)^{1/2}$ to the viscous relaxation time of the particle $\tau_p = \rho_p d_p^2 / 18 \nu \rho_f$. Since the Kolmogorov time scale increases with time, the Stokes number decreases during the decay, as shown in Fig. 12. The Stokes number is close to one, thus the particles will respond to turbulent motion while behaving differently from the fluid. Indeed, for Stokes numbers of the order of 1 the particle–turbulence interaction is enhanced (Bosse et al. 2006; Squires and Eaton 1991; Ferrante and Elghobashi 2003).

The simultaneous velocimetry technique allows the measurement of the velocities of the particles and the surrounding flow. The measured velocity field of the fluid at time t is written as $\mathbf{u}_f(\mathbf{x}, t)$. The velocity of a particle is written as $\mathbf{u}_p(\mathbf{x}_p)$, where \mathbf{x}_p is the position of the particle. The closest measured fluid velocity vector is written $\mathbf{u}_{fp}(\mathbf{x}, t)$. These vectors are represented in Fig. 13. The maximal distance between a particle and the nearest fluid velocity vector is 1.1 mm, and this separation is of the order of the particles diameter.

The probability density function (PDF) of the components of \mathbf{u}_f , \mathbf{u}_p and \mathbf{u}_{fp} at two different stages of the decay are presented in Fig. 14. The PDF of the fluid velocity, \mathbf{u}_f , and the fluid velocity at particle locations, \mathbf{u}_{fp} , is close, suggesting that the particles sample homogeneously the fluid flow field. In addition, \mathbf{u}_f and \mathbf{u}_p exhibit similar statistics at a different stages of the decay.

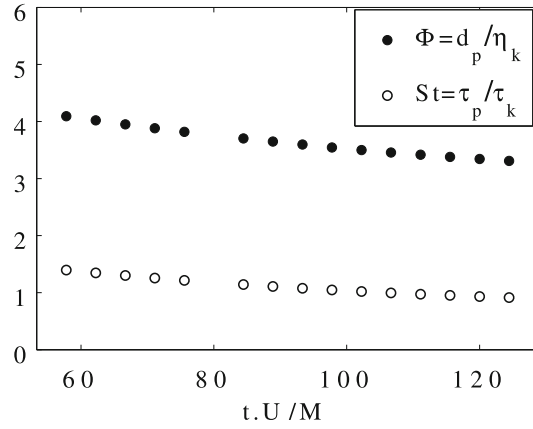


Fig. 12 Comparison between particle scales and turbulence scales: Φ is the ratio of the particles diameter, d_p to the Kolmogorov length scale, η_k . The Stokes number St is the ratio of the particle viscous relaxation time, τ_p to the Kolmogorov time scale, τ_k

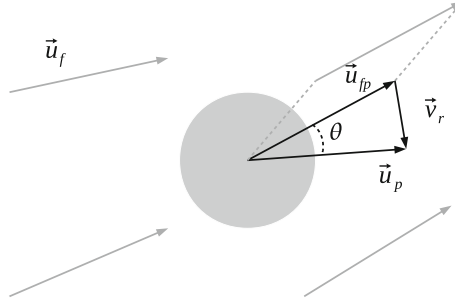


Fig. 13 Particle velocity \mathbf{u}_p is compared with the nearest fluid velocity vector \mathbf{u}_{fp} , by computing the relative velocity \mathbf{v}_r and the angle θ between the two vectors. The other fluid velocity vectors in the flow field are written as \mathbf{u}_f

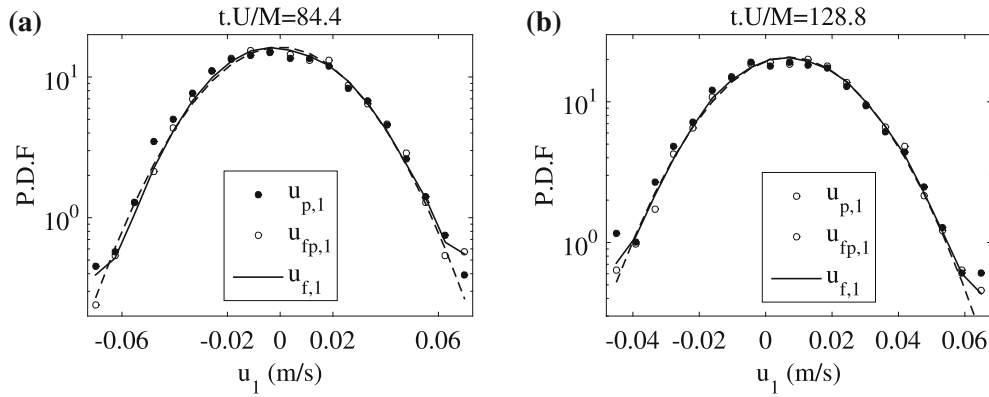


Fig. 14 PDFs of the particles and fluid velocities along the x axis: $u_{p,1}$ is particle velocity, $u_{fp,1}$ is fluid velocity near the particle position, $u_{f,1}$ is the non-local fluid velocity, and the dashed line represents a Gaussian distribution with the same mean and variance

A closer examination of the velocity statistics reveals differences between the particles and the fluid flow dynamics. Since we have access to both phases velocities, we can locally compute the relative velocity between the two phases $\mathbf{v}_r = \mathbf{u}_p - \mathbf{u}_{fp}$. In Fig. 15, we show the PDF of the normalized first component (along the x direction) of the relative velocity $v_{r,1}/\langle u_{fp,1}^2 \rangle^{1/2}$ at two different stages of the turbulence decay. We notice that the PDFs are weakly skewed and are flatter than a normal distribution. The PDF kurtosis is estimated to be always larger than 10, although the available number of realizations is not sufficiently large to yield exact estimations of high statistical moments. The shape of the PDF shows the intermittent nature of

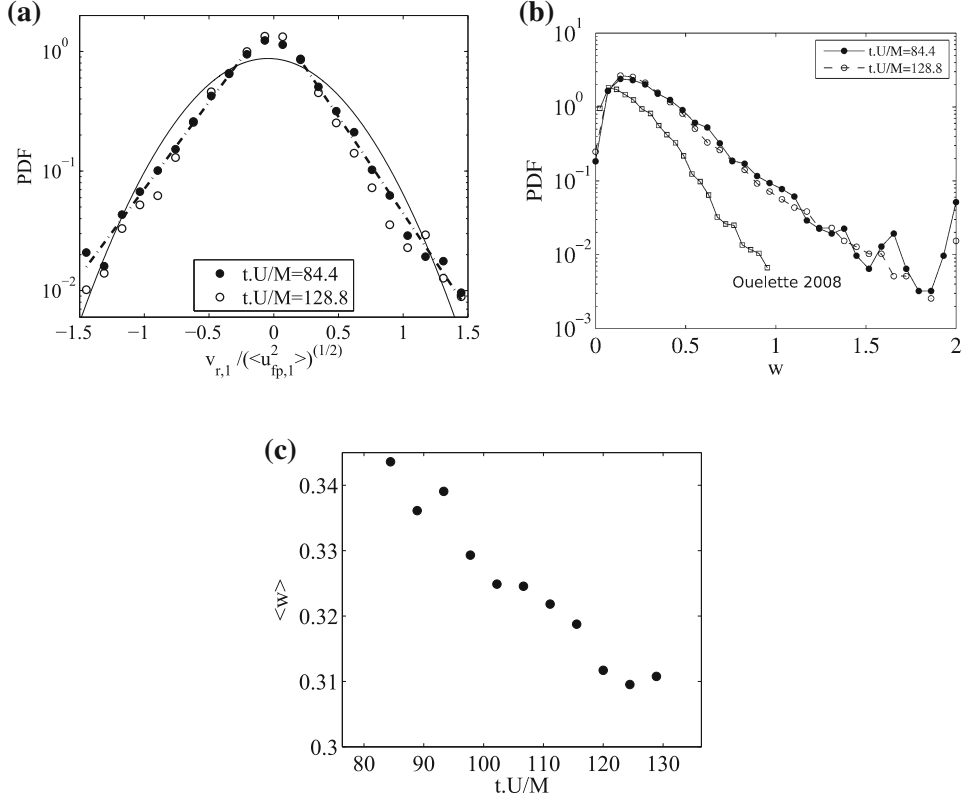


Fig. 15 **a** PDF of the normalized relative velocity at two stages of the decay. The continuous line represents a Gaussian distribution with the same mean and variance. **b** PDF of the normalized relative velocity norm $w = \|\mathbf{u}_p - \mathbf{u}_{fp}\| / \langle \|\mathbf{u}_{fp}\| \rangle$ at two stages of the decay with comparison to results from Ouellette et al. (2008) (open square). **c** Temporal decay of the average relative velocity norm

the two phase velocity differences: mainly, the particles follow well the surrounding flow, but large departure from local fluid velocities occurs with a finite probability. In addition, the PDF's tails are well approximated by an exponential distribution. This feature is shared with the PDFs of Eulerian spatial or temporal fluid velocity increments in turbulent flows (Monin and Yaglom 1975). Moreover, the comparison of the normalized PDFs at two stages of the decay shows that the shape does not change significantly throughout the decay. This observation suggests that the local velocity differences are self-similar throughout the decay.

The inspection of the PDF values shows that, although the most probable value of velocity differences is zero, significant two phase velocity differences occur with a finite, non-negligible probability. From the assumption of exponential tails for the PDF, one can show that the particles have a probability of 19 % to have a relative velocity equal to or larger than half of the r.m.s of the fluid velocity, which corresponds to a displacement close to 2.5 pixels. Thus, the values of the velocity discrepancy between the two phases are non-negligible and cannot be solely due to measurement bias.

In Fig. 15b, we show the PDF of the normalized norm of the relative velocity $w = \|\mathbf{u}_p - \mathbf{u}_{fp}\| / \langle \|\mathbf{u}_{fp}\| \rangle$ at two different stages of the decay. The results from Ouellette et al. (2008) are also presented in this figure. We find clear evidence that the particles behave differently from the surrounding fluid. In addition, our results are consistent with the observations of Ouellette et al. (2008) who show that finite-size particle motion is different from the underlying flow. In our experiments, the PDF has larger tails. Thus, the probability of having larger relative velocity differences is higher. This is most probably due to the differences between the two experiments. While in ours, the flow is three dimensional and fully turbulent, in Ouellette et al. (2008) experiments, the particles are embedded in a two-dimensional chaotic flow. The values of w against time are shown in Fig. 15c. These values are clearly decreasing during the turbulence decay.

The above-highlighted velocity differences may originate from a difference of velocity norm between the particles and the surrounding fluid defined by $\delta u = (\|\mathbf{u}_p\| - \|\mathbf{u}_{fp}\|) / \langle \|\mathbf{u}_{fp}\| \rangle$. The velocity difference

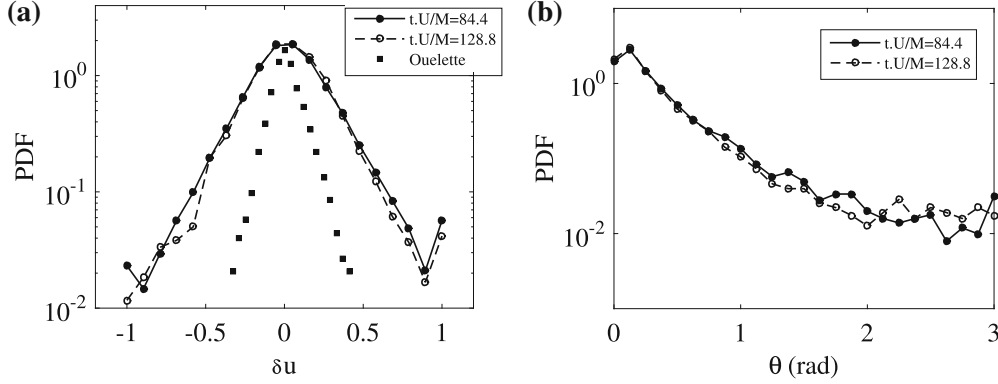


Fig. 16 **a** Velocity norm difference $\delta u = (\|\mathbf{u}_p\| - \|\mathbf{u}_{fp}\|) / \langle \|\mathbf{u}_{fp}\| \rangle$ PDF at two stages of the decay with comparison to Ouellette et al. (2008) (filled square). **b** The angle $\theta = (\mathbf{u}_p, \mathbf{u}_{fp})$ PDF at two stages of the decay

may also be due to a misalignment of the two velocity vectors; this is defined by the angle θ between \mathbf{u}_p and \mathbf{u}_{fp} . The PDFs of δu and θ are represented in Fig. 16 and compared with Ouellette’s results.

The PDFs of δu at the two stages of the decay are symmetrical, showing that the particles are equally likely to move slower or faster than the surrounding fluid. The PDF of θ shows that the particles have a finite probability to move in a direction different from that of the fluid. In fact, the particles have an estimated probability of 16 % to move with an angle larger than $\pi/6$ from the direction of the motion of the surrounding fluid. Therefore, the velocity differences between the two phases are both due to velocity norm differences and misalignment of the velocity vectors.

In the following, we discuss the possible origins of the observed two phase velocity differences. As shown previously, a major feature of the velocity differences statistics is their intermittency. This suggests a link with other intermittent quantities in turbulent flows, such as acceleration or Eulerian velocity increments. If the particle inertia prevails, then the velocity differences are proportional to the particle acceleration, as shown by the Stokes equation. On the other hand, if the finite-size effect prevails, then the velocity differences are proportional to the velocity Laplacian (Homann and Bec 2010). Both quantities are intermittent, since they involve temporal or spatial derivative of the fluid velocity. In their study, Ouellette et al. (2008) suggest that the difference is due to the inertial behavior of the particles. We rule out this explanation in our case, since, as shown by Homann and Bec (2010) and Calzavarini et al. (2012), the inertial effects are not dominant on the dynamics of neutrally buoyant finite-size particles in turbulence, but rather the finite-size effects (i.e., spatial filtering).

If both temporal and spatial filtering effects are weak, the particles then behave mainly as tracers. In this case, the difference may be attributed to the fact that the velocities are not measured at the same location. Thus, the velocity differences may be velocity spatial increments for separations equal to the distance between a particle centroid and the closest fluid velocity vector position. This difference increases with the local velocity gradients of the flow. In addition, the filtering effect of the PIV may also introduce a difference in velocity between the two phases. If the particles behave as tracers, then velocity discrepancy is comparable to a difference between a local value of the fluid velocity and the spatially averaged fluid velocity. This difference, when it exists, is a result of finite velocity gradient inside the pattern box.

5 Conclusions

In this article, the velocities of finite-size, neutrally buoyant particles embedded in a turbulent flow have been measured and compared with that of the neighboring flow using a simultaneous velocimetry set-up combining the PIV technique (for the fluid phase) and PTV technique (for the particles). This set-up and the relevant post-processing techniques have been described and discussed.

The implementation of this set-up is particularly challenging, mainly due to the relatively large size of the solid particles. The scatter of the fluorescent emission by the particles is not negligible because of their large area. Therefore, additional post-processing is required to distinguish between the two phases in the PIV images. In addition, several issues specific to large particles detection and localization have been addressed. The change of the particle images shapes between two successive camera frames has been

identified as a major source of errors on the displacement measurements. New post-processing procedures have been proposed to alleviate these problems, and the feasibility of the simultaneous velocimetry for large particles has been confirmed.

From the results of the simultaneous measurements, the velocity statistics of the two phase have been investigated. The velocity statistics of the two phases have been shown to be close. However, significant local velocity differences between the two phases have been found to occur with a finite probability. The average velocity difference between the two phases has been found to be significant and larger than accumulated bias from both PIV and PTV measurements.

References

- Adrian RJ (1997) Dynamic ranges of velocity and spatial resolution of particle image velocimetry. *Meas Sci Technol* 8(12):1393
- Adrian RJ, Westerweel J (2011) Particle image velocimetry, vol 30. Cambridge University Press, Cambridge
- Aliseda A, Cartellier A, Hainaux F, Lasheras JC (2002) Effect of preferential concentration on the settling velocity of heavy particles in homogeneous isotropic turbulence. *J Fluid Mech* 468:77–105
- Balachandar S, Eaton JK (2010) Turbulent dispersed multiphase flow. *Annu Revi Fluid Mech* 42:111–133
- Bec J, Biferale L, Boffetta G, Celani A, Cencini M, Lanotte A, Musacchio S, Toschi F (2006) Acceleration statistics of heavy particles in turbulence. *J Fluid Mech* 550:349–358
- Blois G, Barros JM, Christensen KT (2015) A microscopic particle image velocimetry method for studying the dynamics of immiscible liquid-liquid interactions in a porous micromodel. *Microfluid Nanofluidics* 18(5–6):1391–1406
- Bosse T, Kleiser L, Meiburg E (2006) Small particles in homogeneous turbulence: settling velocity enhancement by two-way coupling. *Phys Fluids* 18(2):027102
- Calzavarini E, Volk R, L  v  que E, Pinton JF, Toschi F (2012) Impact of trailing wake drag on the statistical properties and dynamics of finite-sized particle in turbulence. *Phys D Nonlinear Phenom* 241(3):237–244
- Charonko JJ, Vlachos PP (2013) Estimation of uncertainty bounds for individual particle image velocimetry measurements from cross-correlation peak ratio. *Meas Sci Technol* 24(6):065301
- Elhimer M, Jean A, Praud O, Bazile R, Marchal M, Couteau G (2011) Dynamics of finite size neutrally buoyant particles in isotropic turbulence. In: *Journal of Physics: Conference Series*, vol 318. IOP Publishing, Bristol, pp 052004
- Fernando, HJS, De Silva IPD (1993) Note on secondary flows in oscillating-grid, mixing-box experiments. *Phys Fluids A Fluid Dyn* (1989–1993) 5(7):1849–1851
- Ferrante A, Elghobashi S (2003) On the physical mechanisms of two-way coupling in particle-laden isotropic turbulence. *Phys Fluids* 15(2):315–329
- Fincham AM, Delerce G (2000) Advanced optimization of correlation imaging velocimetry algorithms. *Exp Fluids* 29(1):S013–S022
- Fincham AM, Spedding GR (1997) Low cost, high resolution dpiv for measurement of turbulent fluid flow. *Exp Fluids* 23(6):449–462
- Fincham AM, Spedding GR, Blackwelder RF (1991) Current constraints of digital particle tracking techniques in fluid flows. *Bull Am Phys Soc* 36:2692
- Hagiwara Y, Murata T, Tanaka M, Fukawa T (2002) Turbulence modification by the clusters of settling particles in turbulent water flow in a horizontal duct. *Powder Technol* 125(2):158–167
- Homann H, Bec J (2010) Finite-size effects in the dynamics of neutrally buoyant particles in turbulent flow. *J Fluid Mech* 651:81
- Keane RD, Adrian RJ (1990) Optimization of particle image velocimeters. i. double pulsed systems. *Meas Sci Technol* 1(11):1202
- Khalitov DA, Longmire EK (2002) Simultaneous two-phase piv by two-parameter phase discrimination. *Exp Fluids* 32(2):252–268
- Kiger KT, Pan C (2000) Piv technique for the simultaneous measurement of dilute two-phase flows. *J Fluids Eng* 122(4):811–818
- Lu J, Nordsiek H, Shaw RA (2010) Clustering of settling charged particles in turbulence: theory and experiments. *New J Phys* 12(12):123030
- Mohamed MS, Larue JC (1990) The decay power law in grid-generated turbulence. *J Fluid Mech* 219(-1):195
- Monchaux R, Bourgoin M, Cartellier A (2012) Analyzing preferential concentration and clustering of inertial particles in turbulence. *Int J Multiph Flow* 40:1–18
- Monin AS, Yaglom AM (1975) Statistical fluid mechanics: mechanics of turbulence, vol 2. MIT Press, Cambridge, p 874
- Morize C, Moisy F, Rabaud M (2005) Decaying grid-generated turbulence in a rotating tank. *Phys Fluids* 17(9):5105
- Ouellette NT, Malley PJJO, Gollub JP (2008) Transport of finite-sized particles in chaotic flow. *Phys Rev Lett* 101(17):174504
- Poelma C (2004) Experiments in particle-laden turbulence: simultaneous particle/fluid measurements in grid-generated turbulence using particle image velocimetry. PhD thesis, TU Delft, Delft University of Technology
- Poelma C, Westerweel J, Ooms G (2006) Turbulence statistics from optical whole-field measurements in particle-laden turbulence. *Exp Fluids* 40(3):347–363
- Poelma C, Westerweel J, Ooms G (2007) Particle-fluid interactions in grid-generated turbulence. *J Fluid Mech* 589(1):315–351
- Qureshi NM, Bourgoin M, Baudet C, Cartellier A, Gagne Y (2007) Turbulent transport of material particles: an experimental study of finite size effects. *Phys Rev Lett* 99(18):184502

- Schmitt FG, Seuront L (2008) Intermittent turbulence and copepod dynamics: increase in encounter rates through preferential concentration. *J Mar Syst* 70(3):263–272
- Sciacchitano A, Neal DR, Smith BL, Warner SO, Vlachos PP, Wieneke B, Scarano F (2015) Collaborative framework for PIV uncertainty quantification: comparative assessment of methods. *Meas Sci Technol* 26(7):074004. ISSN:0957-0233
- Spedding GR, Rignot EJM (1993) Performance analysis and application of grid interpolation techniques for fluid flows. *Exp Fluids* 15(6):417–430
- Squires KD, Eaton JK (1991) Preferential concentration of particles by turbulence. *Phys Fluids A Fluid Dyn* 3(5):1169
- Takehara K, Etoh T (1999) A study on particle identification in ptv particle mask correlation method. *J Vis* 1(3):313–323
- Vignal L (2006) Chute d'un nuage de particules dans une turbulence diffusive. Etude des couplages entre phases par diagnostics optiques. PhD thesis, Institut National Polytechnique de Toulouse
- Weil JC, Sykes RI, Venkatram A (1992) Evaluating air-quality models: review and outlook. *J Appl Meteorol* 31(10):1121–1145
- Yoshimoto H, Goto S (2007) Self-similar clustering of inertial particles in homogeneous turbulence. *J Fluid Mech* 577:275